Study of slip activity in a Mg-Y alloy by in situ high energy X-ray diffraction microscopy and elastic viscoplastic self-consistent modeling

Leyun Wang[1,2*], Zhonghe Huang[1], Huamiao Wang[3], Alireza Maldar[1], Sangbong Yi[4], Jun-Sang Park[5], Peter Kenesei[5], Erica Lilleodden[2], Xiaoqin Zeng[1,6*]

[1] National Engineering Research Center of Light Alloy Net Forming and State Key Laboratory of Metal Matrix Composites, School of Materials Science and Engineering, Shanghai Jiao Tong University, Shanghai 200240, China

[2] Institute of Materials Research, Helmholtz-Zentrum Geesthacht, 21502 Geesthacht, Germany

[3] State Key Laboratory of Mechanical System and Vibration, Shanghai Jiao Tong University, Shanghai 200240, China

[4] Magnesium Innovation Centre, Helmholtz-Zentrum Geesthacht, 21502 Geesthacht, Germany

[5] Advanced Photon Source, Argonne National Laboratory, Lemont, IL 60439, USA

[6] Shanghai Innovation Institute for Materials, Shanghai, 200444, China

*Corresponding author

Email: leyunwang@sjtu.edu.cn and xqzeng@sjtu.edu.cn

Abstract

Slip activity from various slip modes largely determines the yield strength and ductility of Mg alloys. Solid solution elements in Mg can change the slip activity dramatically. In this paper, far-field high energy X-ray diffraction microscopy (FF-HEDM) is employed to study slip activity in a Mg-3wt%Y alloy during an in situ tensile experiment. The specimen was incrementally loaded up to 3% engineering strain along the rolling direction. At each load step, FF-HEDM data were collected to track the crystallographic orientation, center of mass, and stress tensor changes of nearly 1000 grains in the probed volume. By analyzing the change in orientation and stress tensor of individual grains at different load steps, it is possible to identify the activated slip systems and measure their critical resolved shear stress (CRSS) values. Prismatic slip and pyramidal I <a> slip are found to be very active in this alloy. The estimated CRSS values for basal slip, prismatic slip and pyramidal I <a> slip are 12 MPa, 38 MPa, and 36 MPa, respectively. These CRSS values were applied in a dislocation-based elastic viscoplastic self-consistent (EVPSC) model that successfully simulated the tensile stress-strain curve from the FF-HEDM experiment. The model also qualitatively predicted the crystal rotation in most of the selected grains, though it underestimated the internal stress and the magnitude of crystal rotation in these grains. Influence of solute Y on the strength and ductility of Mg alloys is discussed.

Keywords

Mg alloy; Solute strengthening; Dislocations; Synchrotron radiation; EVPSC

1. Introduction

Application of Mg alloys as structural material largely depends on the ongoing efforts to improve their mechanical properties. In recent years, Y-containing Mg alloys have received strong attention, as they often possess a good combination of strength and ductility. Several mechanisms have been proposed to explain the role of Y in Mg alloys. First of all, Y addition apparently weakens the crystallographic texture of Mg alloys after wrought processes [1–3]. Pure Mg typically develops strong basal-type textures after rolling or extrusion, with most grains having their basal plane parallel to the rolling direction (RD) or the extrusion direction (ED). Such a texture inhibits the activation of both $\{0001\}<11\bar{2}0>$ basal slip and $\{10\bar{1}2\}<\bar{1}011>$ twinning under tension along RD or ED, resulting in low strain to failure along these two directions. When small amount of Y is added, the basal-type textures of Mg are often weakened. This can partly explain the ductility improvement in Mg-Y. On the other hand, the yield strength of Mg-Y being higher than pure Mg indicates that solute Y probably changes the deformation behavior of Mg intrinsically [4]. According to density functional theory (DFT) studies, solute Y lowers the basal stacking fault energy (SFE) in Mg [5–8]. Sandlöbes et al. [5, 6] observed a large number of <c+a> dislocations in the vicinity of basal stacking faults in cold rolled Mg-3wt%Y alloys. Based on that observation, they attributed the high ductility of Mg-Y to the easily formed basal stacking faults that enable heterogeneous nucleation of <c+a> dislocations. This explanation, however, was challenged in a few latest papers. For example, Zhang and Lavernia [9] observed very few <c+a> dislocations

after room temperature tension and compression of a Mg-2.5wt%Y extruded alloy despite the presence of many basal stacking faults. It was thus suggested by the authors that the previously reported <c+a> dislocations in Mg-Y might be a result of the complex stress state during rolling, and the role of <c+a> slip on the tensile ductility in Mg-Y may be limited [9]. Using DFT based calculation, Yin and Curtin [10] compared the effect of solute Y, Al, and Zn on basal and pyramidal II stacking fault energies. Their calculation shows that while Y does reduce SFEs on these two planes, the same effect can also be achieved by solute Al or Zn at a higher concentration below their respective solubility limit. Since most Mg-Al and Mg-Zn alloys do not show a strong <c+a> dislocation activity during their deformation, the reduced SFE may not be the key reason for the observed <c+a> dislocation activity and the enhanced ductility in Mg-Y [10].

Using first-principles calculation [11, 12] or crystal plasticity modeling [13, 14], some authors began to directly assess the effect of solute Y on the critical resolved shear stress (CRSS) values of individual slip and twin modes in Mg. Kim et al. [12] reported that Y increases the CRSS for all slip modes, but the strengthening effect on basal and prismatic slip is more pronounced than that on <c+a> slip. Consequently, <c+a> slip is predicted to be more active in Mg-Y. In contrast, Stanford et al. [14] reported that Y strengthens <c+a> slip more strongly than basal slip based on in situ neutron diffraction experiment and elastoplastic self-consistent (EPSC) modeling. In light of these contradictory conclusions, further investigation is necessary to

quantitatively interrogate the influence of Y on the CRSS values of different slip modes and understand the ductility improvement in Mg-Y alloys.

In the present paper, in situ far-field high energy X-ray diffraction microscopy (FF-HEDM) is employed to study the deformation behavior of Mg-3wt%Y alloy. FF-HEDM, also known as three-dimensional X-ray diffraction (3DXRD), can be used to characterize the micromechanical state of individual grains in polycrystalline materials [15–18]. In a typical FF-HEDM setup, high energy monochromatic X-ray beam illuminates the entire cross section of the specimen and an area detector is placed approximately 1 m away from the specimen. Diffraction spots from all grains that satisfy the Bragg's condition are recorded by the area detector while the specimen is rotated with respect to the incoming X-ray beam. These diffraction spots are used to determine the crystallographic orientations and centers of mass (COMs) of the constituent grains in the illuminated volume as well as their elastic strain states. Various analysis strategies exist to efficiently analyze the data [17–23]. By repeating the analysis for consecutive load steps during an in situ test, deformation history in individual grains can be tracked. The FF-HEDM technique has been used to study grain-level stress heterogeneity and stress relaxation [24–27], twin nucleation [28–31], and slip activity [32–36] in different materials.

In this work, we tracked the deformation of nearly 1000 grains in a Mg-Y alloy specimen. By following the orientation rotation, activities of $\{0001\}<11\bar{2}0>$

basal slip, $\{1\bar{1}00\}<11\bar{2}0>$ prismatic slip, and $\{1\bar{1}01\}<11\bar{2}0>$ pyramidal I <a> slip were identified in different grains. Combined with the stress tensor in these grains obtained from FF-HEDM, the CRSS values for the corresponding slip modes were estimated. The experimentally-determined CRSS values were used in an elastic viscoplastic self-consistent (EVPSC) model with dislocation-based constitutive law. The simulation results were compared with the experimental data in terms of macroscopic stress-strain curve, relative activity of different deformation modes, and the evolution of internal stress and crystal rotation in selected grains.

2. Experimental and modelling procedures

2.1 Material and in situ FF-HEDM experiment

A binary Mg-3wt%Y alloy was produced by melting pure Mg and pure Y. Slabs with a thickness of 20 mm were machined for rolling trials. The slabs were rolled at 450 °C to the thickness of 1.5 mm with 20% of the pass reduction degree. During the hot rolling, the rolled sheets were annealed for 10 min after each rolling step. The hot rolled sheets were subsequently rolled at room temperature to the thickness of 1.0 mm, with 3 ~ 5% pass reduction degree to avoid cracking. The rolled sheets in the final state were annealed at 500 °C for 1 h. The average grain size after final annealing was approximately 50 μm. In-plane tensile specimens with the gauge dimension of 4 mm×1 mm×1 mm (L×W×T) were fabricated from the rolled sheet, with the tensile axis being parallel to the RD.

In situ FF-HEDM experiment was conducted at the Advanced Photon Source (APS) beamline 1-ID-E as illustrated in Fig. 1(a). The detailed setup of the beamline can be found in [37]. A 100 μm tall by 1.5 mm wide monochromatic X-ray beam (energy=52.0 keV, λ=0.0238 nm) illuminated the entire cross section of the specimen. A customized compact load frame was mounted on a rotation stage and the loading axis was aligned to the rotation axis (**Z**). The load frame and the specimen were rotated about the tensile axis (Z//RD) over a 360° range while a diffraction pattern was recorded on an amorphous Si area detector (GE 41RT) at every 0.25° rotation interval (i.e. a total of 1440 diffraction patterns per measurement). The exposure time for each diffraction pattern was 0.3 s. The specimen-to-detector distance was approximately 830 mm determined using NIST standard CeO_2 powder. The specimen was deformed incrementally by uniaxial tension with 23 steps to about 3.0% strain. After each incremental loading and a waiting time of about 30 sec, a FF-HEDM measurement was performed while the displacement of the load frame crosshead was held constant during the specimen rotation. This measurement took about 25 min at each step and the load relaxed only slightly during this holding time. Fig. 1(b) shows the stress-strain curve from the in situ experiment, in which the solid symbols represent the immediate flow stress in the specimen after each loading, and the open symbols represent the stress readout after the FF-HEDM measurement of each step. Stress relaxation was negligible in the elastic stage and up to 6 MPa at 3% strain. Stress relaxation during the FF-HEDM was always below 2 MPa, as the majority of the stress relaxation occurred in the first few seconds after each loading

during the waiting time [27]. Given that, it is reasonable to assume that the stress states in individual grains were nearly constant during the HEDM measurement at each deformation step. A digital image correlation (DIC) camera was used to ensure that the same location on the specimen gauge was illuminated at all deformation steps, which is critical for tracking approximately the same set of grains through the test.

2.2 Grain indexing

After the experiment, grain indexing was performed using the diffraction patterns and the MIDAS software package developed at the APS [38–40]. Due to its robust definition of the experimental setup that closely matches the physical setup at the APS 1-ID-E beamline, ability to address overlapped diffraction spots, and parallelization capability, MIDAS allowed us to identify a large number of grains (>1000 grains) and determine their orientations, COMs, grain radius, and strain tensors with over 90% completeness. Estimated mean errors for the crystal orientation, COM position, and strain tensor components are 0.1°, 10 μm, 5×10^{-5}, respectively for the underformed material. The elastic strain tensors were transformed to stress tensors using generalized Hooke's Law and the following elastic constants of Mg: C_{11}=59.75 GPa, C_{33}=61.7 GPa, C_{44}=16.39 GPa, C_{12}=23.24 GPa, C_{13}=21.7 GPa [41]. For each grain, this stress tensor, rather than the global uniaxial stress, was used to compute the resolved shear stress (RSS) on different slip systems.

2.3 Elastic viscoplastic self-consistent modeling

In this work, we use the EVPSC model developed by Wang et al. [42] to simulate the tensile deformation behavior of this material. Compared with the viscoplastic self-consistent (VPSC) framework [43], the EVPSC model takes elastic deformation into account and is able to predict not only macroscopic stress-strain response and texture evolution but also the development of lattice strain, making it very compatible with in situ synchrotron or neutron experiments [44–46].

For the EVPSC formulation, incremental deformation of the material is obtained using a self-consistent approach, where each grain (single crystal) is treated as an ellipsoidal Eshelby inclusion embedded in a homogeneous effective medium that has the properties of the bulk material. The plastic strain rate in a single crystal, $\dot{\varepsilon}^p$, is composed of the shear rates of all deformation mechanisms:

$$\dot{\varepsilon}^p = \sum_\alpha \dot{\gamma}^\alpha \mathbf{m}^\alpha \tag{1}$$

where $\mathbf{m}^\alpha$ and $\dot{\gamma}^\alpha$ are the Schmid tensor and the shear rate of deformation system α. If α is a slip system,

$$\dot{\gamma}^\alpha = \dot{\gamma}_0 \left(\frac{\mathbf{m}^\alpha : \boldsymbol{\sigma}}{\tau_s^\alpha} \right)^n \operatorname{sgn}\left(\mathbf{m}^\alpha : \boldsymbol{\sigma}\right) \tag{2}$$

where $\boldsymbol{\sigma}$, $\dot{\gamma}_0$, n, τ_s^α, sgn are grain-averaged stress tensor, reference shear rate, power law exponent, critical resolved shear stress for slip system α, and signum function to determine the direction of shear, respectively. A dislocation-based constitutive law is employed to update the value of τ_s^α [47]:

$$\tau_s^\alpha = \tau_0^\alpha + \chi \mu b^\alpha \sqrt{\rho^\alpha} \tag{3}$$

where τ_0^α, χ, μ, b^α, and ρ^α are the initial CRSS, dislocation interaction coefficient, directional shear modulus, Burgers vector length, and dislocation density for system α. Evolution of the dislocation density ρ^α is further described by the following equations [47]:

$$\frac{d\rho^\alpha}{d\gamma^\alpha} = k_1^\alpha \sqrt{\rho^\alpha} - k_2^\alpha \rho^\alpha \tag{4}$$

$$\frac{k_2^\alpha}{k_1^\alpha} = \frac{\chi b^\alpha}{g^\alpha}\left(1 - \frac{kT}{D^\alpha (b^\alpha)^3}\ln\left(\frac{\dot{\varepsilon}}{\dot{\varepsilon}_0}\right)\right) \tag{5}$$

where k_1^α is a rate-insensitive coefficient for dislocation storage by statistical trapping of mobile dislocation, k_2^α is a rate-sensitive coefficient that accounts for dynamic recovery, g^α is a normalized, stress-independent activation energy, D^α is a drag stress, k is the Boltzman's constant (=1.38×10^{-29} MPa m^3/K), $\dot{\varepsilon}_0$ is a reference strain rate (= 10^7 s^{-1}), respectively.

If α is a twinning system, a twinning-detwinning (TDT) scheme [48] is employed. In this case, $\dot{\gamma}^\alpha$ is analogous to Eq. (2) if the resolved shear stress is in the right direction for twinning to occur; otherwise, $\dot{\gamma}^\alpha$ is zero. Because twinning is generally suppressed in this loading condition, we assume τ_s^α does not evolve with strain (i.e. $\tau_s^\alpha = \tau_0^\alpha$) for twinning.

The initial 955 grain orientations obtained from the FF-HEDM experiment at step 0 are used to represent the undeformed specimen. The loading history of the specimen is simulated by uniaxial tension along RD. Five deformation modes, namely basal,

prismatic, pyramidal I <a>, $\{11\bar{2}2\}<\bar{1}\bar{1}23>$ pyramidal II <c+a> slip, and $\{10\bar{1}2\}<\bar{1}011>$ twinning were included in the simulation.

3. Results

3.1 Grain identification and tracking

Grain indexing using MIDAS was performed for the first 15 deformation steps (steps 0–14) up to 0.85% strain. 955 grains were successfully indexed at step 0 (after mounting the specimen in the compact load frame, before loading). Fig. 2(a) shows the {0002} pole figure based on the orientations of these grains. The specimen exhibits a basal-type texture with most of the {0002} poles aligned close to the normal direction (ND//X). However, the maximum intensity of the basal pole figure is approximately 4 multiples of uniform distribution (MUD), which is significantly lower than that of pure Mg of similar processing history (more than 10 MUD, e.g. [49]). The number of grains at subsequent steps slightly varies around 1000. For example, the number of indexed grains at step 7 (ε=0.14%), step 11 (ε=0.46%), step 14 (ε=0.85%) are 1044, 1046, and 972, respectively. This variance is understandable given that the probed volume might be slightly different between different load steps. In addition to crystal orientation, COMs and elastic strain tensors of the indexed grains at each load step are also computed by MIDAS.

To study the deformation history of individual grains, a key procedure is tracking the same grains through different deformation steps. This is achieved by using both

crystallographic orientation and COM information: a grain in step 0 is recognized in step N (N=1−14) if the total change of grain orientation is less than 1° and the COM distance is less than 30 μm. Using this relatively restricted criterion, a total of 286 grains (i.e. ~30% of the indexed grains) were successfully tracked over most deformation steps. Fig. 2(b) shows the {0002} poles of these 286 grains. Ten grains that show distinct evidence of basal slip, prismatic slip, or pyramidal I <a> slip are highlighted. Detailed analysis of the slip activity in these grains and further estimation of CRSS values will be given in the next sections.

Fig. 3 shows the COMs of the tracked 286 grains at four load steps. Each dot denotes the COM of a grain and its color denotes the von Mises stress (σ_{VM}) associated with the grain computed from grain stress tensor at corresponding load steps. The COMs of these grains are scattered within the probed material volume (1000 μm×1000 μm×100 μm) by the X-ray beam. At load step 0, the specimen shows relatively low levels of residual stress. Upon loading, σ_{VM} in all grains increased and became more heterogeneous from grain to grain. This is a typical behavior during plastic deformation of polycrystals due to the different deformation history in different grains induced by anisotropic mechanical property and complex boundary conditions at the grain length scale. To explore potential factors that lead to this stress heterogeneity, the variation of σ_{VM} as a function of grain radius (output by FF-HEDM) and the variation of σ_{VM} as a function of the angle between the grain's c-axis and the Z direction (i.e. c-axis tilt) are plotted in Fig. 4 and Fig. 5, respectively. The mean

value and standard deviation of σ_{VM} both increased significantly from step 0 to step 7 (ε=0.14%). From Fig. 4, there is almost no trend between σ_{VM} and the grain radius. In contrast, a positive relationship between σ_{VM} and c-axis tilt of a grain is identified in Fig. 5. Grains with their c-axis near 90° from the tensile axis Z tend to develop higher σ_{VM} during deformation. This behavior is related to prismatic slip activity and will be discussed in Section 4.2.

3.2 Grains deformed by prismatic slip

To analyze the orientation rotation and slip activity in a grain during deformation, we define "disorientation" and "c-axis misalignment" as following: for each grain, its "disorientation" at step N is the scalar angular difference in crystal orientation between step N and step 0; its "c-axis misalignment" at step N is the angular change of the <0001> direction between step N and step 0.

Fig. 6 shows the development of disorientation and c-axis misalignment for Grains 47, 83, 219, and 266. The disorientation and c-axis misalignment values increased by almost the same amount in each grain during elastic deformation stage (ε<0.1%). After that, the disorientation value increases continuously with strain, while the c-axis misalignment value changed very little. This behavior indicates that Grains 47, 83, 219, and 266 rotated around their <0001> direction during deformation. According to the crystal plasticity theory [50], activation of a slip system with Burgers vector **b** and slip plane normal **n** would impose both a shear strain and a rotation of the crystal.

The crystal rotation would be around the axis of **t**=**b**×**n**. Among the common slip modes of Mg, only prismatic slip with **b** = $<11\bar{2}0>$ and **n** = $\{1\bar{1}00\}$ will cause a grain to rotate around the <0001> direction. Therefore, it is concluded that Grains 47, 83, 219, and 266 were deformed mainly by prismatic slip. Fig. 6 also shows the evolution of σ_{VM} for each grain. The change of σ_{VM} during loading is generally smooth in these grains.

From the stress tensor and crystal orientation of a grain, it is also possible to compute the resolved shear stress (RSS) on all slip systems. To estimate the CRSS for prismatic slip, evolution of the RSS on the most stressed prismatic slip system (τ_{prism}) as well as the most stressed basal slip system (τ_{basal}), pyramidal I <a> slip system ($\tau_{pyr\ I\ <a>}$), and pyramidal II <c+a> slip system ($\tau_{pyr\ II\ <c+a>}$) were calculated for Grains 47, 83, 219, and 266. Fig. 7 shows the result. Since the three prismatic slip systems will equivalently rotate the grain around the <0001> direction, it is reasonable to assume that the most stressed prismatic slip system (i.e. highest RSS) was activated at the step when the disorientation value started to deviate from the c-axis misalignment value. In Grain 47 (Euler angles ($\varphi1$, Φ, $\varphi2$) = (74°, 91°, 106°)), the most stressed prismatic slip system is $(\bar{1}100)[\bar{1}\bar{1}20]$. This system had higher RSS value (35 MPa) when the grain started to develop prismatic slip (i.e. deviation between the disorientation and c-axis misalignment values) at step 4 (ε=0.11%) than the other two prismatic slip systems (both with RSS about 18 MPa). The RSS value of $(\bar{1}100)[\bar{1}\bar{1}20]$ at step 4 is thus taken as the estimated CRSS for prismatic slip in Grain

47. Note that the RSS values continued to increase in Grain 47 beyond step 4. This indicates that prismatic slip was activated prior to the full yielding of this grain. In a situation when prismatic slip was initially activated in a localized region (e.g. from a grain boundary), the full yielding of the grain could be postponed till higher stress was applied. Same RSS calculations were performed for Grains 83, 219, and 266. The estimated CRSS for prismatic slip in these grains are 49 MPa, 48 MPa, and 52 MPa, respectively. After searching for similar grain rotation behavior in the 286 grains, predominant prismatic slip was identified in a total of 18 grains, and the average CRSS for prismatic slip is 38±9 MPa. Note that this value is significantly lower than the estimated CRSS value (=120 MPa) in [14] using EPSC simulation.

3.3 Grains deformed by basal slip

Texture of this specimen is geometrically unfavorable for the activation of basal slip under tension along the Z direction. Nevertheless, we identify a couple of grains deformed via basal slip based on their orientation rotation. Fig. 8 shows the development of disorientation and c-axis misalignment in Grains 72 and 210. The disorientation and c-axis misalignment values in these two grains increased by almost the same amount throughout the deformation. This observation indicates that the crystal rotations in Grains 72 and 210 were around an axis on the basal plane. Further analysis of the rotation axis by comparing the crystal orientations at step 12 (ε=0.58%) and at step 5 (ε=0.12%) indicates that Grain 72 (Euler angles = (83°, 144°, 47°)) was rotating around $[\bar{1}010]$, which can be caused by the activation of basal slip

system $(0001)[1\bar{2}10]$. Grain 210 (Euler angles = (-34°, 102°, 150°)) was rotating around $[10\bar{1}0]$, which can be caused by the activation of basal slip system $(0001)[\bar{1}2\bar{1}0]$. Fig. 9 shows the evolution of τ_{basal}, τ_{prism}, $\tau_{pyr\ I\ <a>}$, and $\tau_{pyr\ II\ <c+a>}$ in these two grains. In both grains, the identified basal system happened to be the most stressed basal slip system. Assuming these two basal slip systems were activated at step 5 (ε=0.12%), it is estimated that the CRSS for basal slip was 15 MPa in Grain 72 and 9.1 MPa in Grain 210, as shown in Fig. 9. The average CRSS value for basal slip is 12 MPa, which generally agrees with the literature. For example, Agnew et al. [13] reported the CRSS for basal slip in Mg-1.0wt%Y to be 10 MPa; Stanford et al. [14] reported the CRSS for basal slip in Mg-2.2wt%Y to be 17 MPa.

It should be pointed out that pyramidal II <c+a> slip can also cause a grain to rotate around one of the $<1\bar{1}00>$ axes. For example, the observed rotation around $[\bar{1}010]$ in Grain 72 could alternatively result from the activation of $(1\bar{2}12)[1\bar{2}1\bar{3}]$. Likewise, the observed rotation around $[10\bar{1}0]$ in Grain 210 could result from the activation of $(\bar{1}2\bar{1}2)[\bar{1}2\bar{1}\bar{3}]$. The analysis of RSS values, however, suggests that pyramidal II <c+a> slip was unlikely to be the dominant slip mode in these two grains: at step 5, RSS of these two <c+a> systems are found to be -23 MPa and 31 MPa, respectively. These values are much lower than the reported CRSS values for pyramidal II <c+a> slip in the literature (e.g. 170 MPa [13, 14]). Based on that, it is concluded that these two grains were mainly deformed by basal slip rather than pyramidal II <c+a> slip.

3.4 Grains deformed by pyramidal I <a> slip

Fig. 10 shows the development of disorientation and c-axis misalignment for Grains 9, 23, 24 and 211. The disorientation and c-axis misalignment values increased by almost the same amount in each grain till the end of the elastic deformation stage. After that, the disorientation and c-axis misalignment values both increased with strain but by different amounts. Neither prismatic slip nor basal slip can account for this type of orientation rotation. By comparing the crystal orientations at step 12 (ε=0.58%) and at step 7 (ε=0.14%), crystal rotation in Grain 23 during plastic deformation was around an axis of [0.432, -0.099, -0.896] in the crystal coordinate system where a_1//$[2\bar{1}\bar{1}0]$, a_2//$[01\bar{1}0]$, and a_3//[0001]. According to the above theory of **t**=**b**×**n**, activation of pyramidal I <a> slip $(1\bar{1}01)[11\bar{2}0]$ would theoretically cause a grain to rotate around the axis of [0.408, -0.236, -0.882]. The observed rotation axis in Grain 23 being very close to this theoretical value suggests that Grain 23 deformed mainly by this pyramidal I <a> slip system. Pyramidal I <a> slip can also account for the rotation in Grains 9, 23, and 211.

Fig. 11 shows the evolution of τ_{basal}, τ_{prism}, $\tau_{pyr\ I\ <a>}$, and $\tau_{pyr\ II\ <c+a>}$ in Grains 9, 23, 24, and 211. In all of them, the identified pyramidal I <a> system was also the most stressed one among all six pyramidal I <a> slip systems. Assuming pyramidal I <a> slip was activated when the disorientation value started to deviate from the c-axis misalignment value, CRSS for pyramidal I <a> slip in these four grains was estimated

to be 37 MPa, 41 MPa, 34 MPa, and 31 MPa, respectively. The average CRSS value for pyramidal I <a> slip is 36 MPa, which is very close to that for prismatic slip (38 MPa) in this alloy. We will discuss how Y alters the CRSS values of different slip modes of Mg in Section 4.1.

3.5 EVPSC simulation results

EVPSC simulation was conducted using the 955 grain orientations obtained from the FF-HEDM measurement at step 0. The grain radius information obtained from FF-HEDM was used as the volume fraction input of each orientation in the EVPSC model. An ex situ tensile test (continuous loading, strain rate $=5\times10^{-5}$ s^{-1}) using another specimen of this material was additionally conducted. The true stress-strain curve of the ex situ test is generally consistent with the in situ test up to 3% strain (see Fig. 12). From the ex situ stress-strain curve, this Mg-3wt%Y material shows a high work hardening rate and large strain to fracture (> 25%), indicating that Y simultaneously enhances the work hardening ability and ductility of Mg. Fig. 12 shows the simulated stress-strain curve using the parameters listed in Table 1. The measured CRSS values for prismatic, basal and pyramidal I <a> slip are used as the τ_0^α values. The other parameters, including τ_0^α for pyramidal II <c+a> slip and twinning, are calibrated by fitting the experimental stress-strain curves. Fig. 12 shows good agreement between the calculated stress-strain curve by the model and the experimental stress-strain curves from both the in situ test and the ex situ test. Fig. 13(a) shows the relative activities of all five deformation modes as a function of

the applied strain predicted by the model. It is observed that the early deformation (up to 1% strain) was associated with the simultaneous activation of basal, prismatic, and pyramidal I <a> slip modes. This is consistent with our experimental finding that the three slip modes were activated in different grains. The model predicts that the activity of pyramidal I <a> slip would gradually increase with the strain at the cost of reduced basal slip activity. Nevertheless, none of the three slip modes would dominate the deformation. Pyramidal II <c+a> slip activity is predicted to be very low in early deformation and gradually increasing with strain. Twinning is generally suppressed during tension along the RD of the material.

Fig. 13(b) shows the predicted dislocation densities for different slip modes up to 10% macroscopic strain. Dislocation density increased from about 10^{11} m^{-2} (ρ_0^{α} in Table 1) to about 10^{14} m^{-2} for basal, prismatic and pyramidal I <a> slip modes. Pyramidal II <c+a> dislocation density also increased with strain, but at a slower rate. These results were on the same order as the dislocation densities predicted by Wang et al. [46] and measured by Joni et al. [51] for textured AZ31 Mg alloys. The result in Fig. 13 indicates that the plastic deformation of this Mg-3wt%Y material is mainly accommodated by <a> slip on basal, prismatic or pyramidal I planes, while <c+a> slip occurs only in late deformation and has a relatively small contribution to the plasticity.

The measured and simulated disorientation, c-axis misalignment, von Mises stress evolution of Grain 47 and Grain 219 (both deformed by prismatic slip) are compared in Fig. 14(a, b). For Grain 47, the model successfully predicted the crystal rotation around the c-axis, evidenced by a rapid increasing of the disorientation value (black dashed line) while the c-axis misalignment (grey dotted line) was near zero in Fig. 14(a). On the other hand, the model underestimated the magnitude of crystal rotation (i.e. the value of disorientation) even if we discount the crystal rotation in the elastic stage ($\varepsilon<0.1\%$) that likely resulted from some rigid body rotation. The simulated von Mises stress development (blue line) is less than the experimental measurement. Fig. 14(c) shows the calculated evolution of τ_{basal}, τ_{prism}, $\tau_{pyr\ I\ <a>}$, and $\tau_{pyr\ II\ <c+a>}$ in Grain 47. Similar to the experimental finding in Fig. 7, τ_{basal} was very low through the test, and the deformation must be dominated by prismatic slip. For Grain 219, the model predicts that both its disorientation and c-axis misalignment would increase with strain, which is not consistent with the experimental observation in Fig. 6. Fig. 14(d) shows the calculated evolution of τ_{basal}, τ_{prism}, $\tau_{pyr\ I\ <a>}$, and $\tau_{pyr\ II\ <c+a>}$ in Grain 219. The model predicts a relatively high RSS on the basal slip mode (~13 MPa) at the onset of the plastic deformation, enabling its activation along with prismatic slip. In contrast to the simulation result, there was a sharp drop of τ_{basal} after the activation of prismatic slip ($\varepsilon=0.12\%$) in Grain 219, as shown in Fig. 7. This behavior can result from stress redistribution within the grain due to the prismatic slip activation, or from the interaction with neighboring grains. This

change of stress state likely prevented basal slip to be activated in Grain 219. Such events cannot be predicted by the EVPSC model.

Fig. 15 and Fig. 16 show similar simulation results for Grains 72, 210 (both deformed by basal slip) and Grains 23, 211 (both deformed by pyramidal I <a> slip). For these four grains, the model qualitatively predicted the trend of disorientation and c-axis misalignment evolution with strain. Quantitatively, the model underestimated the magnitude of crystal rotation (particularly for Grain 210) and the von Mises stress in all of them. This discrepancy will be discussed in Section 4.2.

4. Discussion

4.1 Effect of Y on the deformation behavior of Mg

For the design of Mg alloys with superior mechanical properties, the higher activities of non-basal deformation modes are critical. Basal slip is usually the most easily activated slip mode regardless of the composition, so those alloying elements that can increase the CRSS of basal slip will generally strengthen the material. The poor ductility of Mg at room temperature is due to the fact that non-basal slip is much more difficult to be activated than the basal slip, so those alloying elements that can reduce the ratio of $CRSS_{non\text{-}basal}/CRSS_{basal}$ will enhance the ductility of the material. The ability to accurately measure the CRSS values of different slip modes is therefore very important for relating individual alloying elements with the mechanical behaviors of Mg alloys. It is not practical, however, to obtain the CRSS values of

individual slip modes by deforming a large single crystalline material, as multiple slip and twinning activities can occur simultaneously during deformation to complicate the analysis. Hence, CRSS values have to be determined using other methods.

One method is using the surface slip lines induced by activation of slip systems. Using grain orientations measured by electron backscattered diffraction (EBSD), it is possible to identify the corresponding slip systems for the observed slip lines. Applying Schmid factor analysis, the relative CRSS ratios between different slip modes can be estimated [52, 53]. This method, however, is based on the assumption that the stress state in each grain is same as the macroscopic applied stress and relies on *surface* observations. As illustrated by other investigators [24–26, 31] and evidenced in this work in Fig. 3, this assumption is inappropriate.

The second method is based on crystal plasticity modeling. The CRSS values of different slip modes are tweaked until experimentally obtained macroscopic stress-strain curves, texture and its evolution, and lattice strains agree with the corresponding simulation results. Quite a few studies use this method to determine CRSS values [4, 13, 14]. On the other hand, this method is sensitive to the constitutive framework as well as the set of slip modes used in the model.

The third method is using micropillar compression inside transmission electron microscope (TEM) or scanning electron microscope (SEM). In such experiments,

single-crystal micropillars with various diameters and crystal orientations are fabricated from polycrystalline Mg alloys using focused ion beam machining and are loaded in uniaxial compression. When surface slip lines or strain burst are observed, CRSS of the corresponding slip systems can be estimated from the instantaneous load on the micropillar [54–57]. This method has been most often used to measure the CRSS for basal slip. Depending on the diameter of the micropillars, $CRSS_{basal}$ in pure Mg were measured to be 50 MPa (at D=1.6 μm) [54], 39–68 MPa (at D=3 μm) [55], 30 MPa (at D=3 μm) [56], and 6 MPa (at D=10 μm) [57]. On the other hand, CRSS for non-basal slip has hardly been reported from micropillar compression tests. Micropillar size effect and free surface effect may also influence the result.

In the present work, we use the FF-HEDM technique to identify slip activity in individual grains from a polycrystalline specimen during a tensile test. According to our measurement, $CRSS_{basal}$ in this Mg-3wt%Y alloy (12 MPa, grain size = 50 μm) is higher than the reported value in pure Mg (6 MPa, micropillar diameter = 10 μm, [56]) and Mg-1wt%Y (10 MPa, grain size = 50 μm, [13]). The comparison indicates that solute Y is able to strengthen Mg by increasing the CRSS of basal slip.

Kula and Niewczas [4] recently studied the room temperature tensile deformation of a rolled Mg-2.92wt%Y specimen using crystal plasticity modeling. They reported the CRSS values for basal, prismatic, pyramidal I <a>, and pyramidal II <c+a> to be 6.7 MPa, 20.1 MPa, 26.8 MPa, and 36.9 MPa, respectively. These values are

systematically lower than the result from the present study (Table 1) due to the grain size difference (186 μm in [4] vs 50μm in the present study). On the other hand, both works report the ratio of $CRSS_{prism}/CRSS_{basal}$ to be around 3.0. This ratio value is lower than that in polycrystalline pure Mg (~5.0) [58]. Pyramidal I <a> slip has long been neglected as a useful deformation mode in Mg alloys. Our study indicates that it may be as active as prismatic slip with $CRSS_{pyr\ I\ <a>}/CRSS_{basal}$ being around 3.0 as well. Overall, it is found that Y reduced the CRSS ratio between non-basal <a> slip and basal slip, thus enhancing the material ductility.

Pyramidal II <c+a> dislocations have been observed by TEM in deformed Mg-Y alloys [4–6, 9]. As shown in [4], those grains where <c+a> dislocations nucleated often contain <a> dislocations in the vicinity as well. Since <c+a> slip has higher CRSS than both basal and non-basal <a> slip, activation of <c+a> slip requires local stress concentration, which can be induced by <a> dislocations' accumulation. Because of the common co-existence of <a> and <c+a> dislocations in the same grain, the method used in this work to identify <a> slip (based on the crystal rotation direction of the entire grain) cannot identify <c+a> slip and measure its CRSS value.

In addition to slip, twinning is another important deformation mode in Mg. In situ HEDM can indeed identify twin nucleation in individual grains in HCP metals [27–31]. Twins are identified as new grains that nucleated after certain amount of plastic deformation, and they must have the theoretical misorientation relationship (i.e.

85° around $<2\bar{1}\bar{1}0>$) with respect to a nearby parent grain. In the present work, no twin nucleation events were identified. This is consistent with the EBSD result in [4]. Two reasons can account for the lack of twin activity. First, the texture of this specimen is unfavorable for twin nucleation as most grains had their c-axis under compression during the tensile test along RD. Secondly, solute Y is known to harden twinning more than its hardening on slip [14]. Even if some twins nucleated, the size of the twins could be too small to be recognized as a grain in indexing. Our EVPSC model also predicts that twinning makes little contribution to the overall plastic deformation (Fig. 13).

4.2 Assessment of heterogeneous deformation at the grain level

Hexagonal metals tend to show strong grain-to-grain heterogeneity when they are subject to deformation. HEDM provides a powerful technique to study heterogeneous deformation in polycrystals. Using FF-HEDM, strong variation of internal stress was observed in polycrystalline Ti and Zr alloys upon loading and after unloading [24, 26, 59–61]. In the present work, strong variation of σ_{VM} among different grains was also observed in this Mg alloy, as shown in Fig. 3. It is further found that those grains whose c-axis is far away from the loading direction (i.e. with large c-axis tilt) tend to develop higher σ_{VM} values, as shown in Fig. 5. When a grain has a c-axis tilt close to 90°, it has a maximum Schmid factor for prismatic slip and a minimum Schmid factor for basal slip. Prismatic slip can be activated in this material, but the CRSS for prismatic slip is still three times of that for basal slip.

Therefore, grains with large c-axis tilt require higher stress for their yielding, which explains the finding in Fig. 5.

In the present work, an EVPSC model has been built using the grains identified by FF-HEDM at step 0 as input. Using the CRSS values obtained in this work, the model successfully simulated the macroscopic stress-strain curve to a large strain level (Fig. 12). Microscopically, the model qualitatively predicted the crystal rotation direction in most of the selected grains. On the other hand, the model underestimated the internal stress and the magnitude of crystal rotation in these grains. This quantitative discrepancy may be originated from two factors. First, the interaction between neighboring grains is considered indirectly in the EVPSC model in terms of the interaction between the grain and the polycrystalline aggregate. The shear effect across grain boundaries that often leads to local stress build-up and orientation rotation is neglected. Second, the model assumes that the initial grains are at zero stress, while in reality most grains had certain level of stress due to either residual stress or preload of the specimen. This discrepancy is attributed by some researchers [26, 62] to explain the difference between the predicted stress using crystal plasticity finite element models (CPFEM) and the measured stress by HEDM at the grain level. While the EVPSC model does not fully capture the local deformation history of individual grains, it yet provides good match for the macroscopic stress-strain curve. Future works will explore some strategy to

incorporate direct interactions among neighboring grains, which might improve the predictability of EVPSC model at the grain level.

5. Conclusions

In situ FF-HEDM was employed to study the tensile deformation along the rolling direction of a Mg-3wt%Y sheet material. This technique allows us to track the deformation history of nearly 1000 grains and identify the activation of different slip modes in those grains where a single slip system dominated. The following conclusions have been drawn:

1. Deformation at the grain level showed strong heterogeneity in terms of internal stress development and grain orientation rotation. During deformation, the von Mises stress (σ_{VM}) of a grain has no obvious correlation with the grain size. On the other hand, σ_{VM} is positively related to the angle between the grain's c-axis and the loading direction.

2. Pure prismatic slip caused a grain to rotate around its c-axis. This behavior was observed in 18 grains. From the calculation of the instantaneous resolved shear stress, the average CRSS for prismatic slip was estimated to be 38 MPa in this alloy.

3. Pure basal slip caused a grain to tilt its c-axis. This behavior was observed in 2 grains. The average CRSS for basal slip was estimated to be 12 MPa. This value is higher than that in pure Mg, confirming the strengthening effect of solute Y in Mg alloys.

4. Pure pyramidal I <a> slip caused a grain to rotate around an axis of [0.408, -0.236, -0.882] or its equivalence in the orthogonal crystal coordinate system. This behavior was observed in 4 grains. The average CRSS for pyramidal I <a> slip was estimated to be 36 MPa.

5. Using the above CRSS values, a dislocation-based EVPSC model is able to simulate the tensile stress-strain curve up to 20% strain for this material. The model also qualitatively predicted the direction of crystal rotation in most of the selected grains, but it underestimated the internal stress and the magnitude of crystal rotation in these grains.

Acknowledgements

This work is financially supported by the National Natural Science Foundation of China (Nos. 51671127 and 51631006). L.W. acknowledges the partial support by the Alexander von Humboldt Foundation and Shanghai Pujiang Program (No 16PJ1404600). Use of the Advanced Photon Source was supported by the United States Department of Energy, Office of Science, Office of Basic Energy Sciences, under Contract No. DE-AC02-06CH11357. We would like to thank Dr. Ricardo Lebensohn and Dr. Carlos Tome of the Los Alamos National Laboratory for access to the use of the VPSC code.

References

[1] J. Bohlen, M.R. Nürnberg, J.W. Senn, D. Letzig, S.R. Agnew, The texture and anisotropy of magnesium–zinc–rare earth alloy sheets, Acta Mater. 55 (2007) 2101–2112.

[2] K. Hantzsche, J. Bohlen, J. Wendt, K.U. Kainer, S.B. Yi, D. Letzig, Effect of rare earth additions on microstructure and texture development of magnesium alloy sheets, Scripta Mater. 63 (2010) 725–730.

[3] A. Imandoust, C.D. Barrett, T. Al-Samman, K.A. Inal, H. El Kadiri, A review on the effect of rare-earth elements on texture evolution during processing of magnesium alloys, J. Mater. Sci. 52 (2017) 1–29.

[4] A. Kula, X. Jia, R.K. Mishra, M. Niewczas, Flow stress and work hardening of Mg-Y alloys, Int. J. Plast. 92 (2017) 96–121.

[5] S. Sandlöbes, S. Zaefferer, I. Schestakow, S. Yi, R. Gonzalez-Martinez, On the role of non-basal deformation mechanisms for the ductility of Mg and Mg–Y alloys，Acta Mater. 59 (2011) 429–439.

[6] S. Sandlöbes, M. Friak, S. Zaefferer, A. Dick, S. Yi, D. Letzig, Z. Pei, L.F. Zhu, J. Neugebauer, D. Raabe, The relation between ductility and stacking fault energies in Mg and Mg-Y alloys, Acta Mater. 60 (2012) 3011–3021.

[7] S. Sandlöbes, Z. Pei, M. Friák, L.F. Zhu, F. Wang, S. Zaefferer, D. Raabe, J. Neugebauer, Ductility improvement of Mg alloys by solid solution: Ab initio modeling, synthesis and mechanical properties, Acta Mater. 70 (2014) 92–104.

[8] S.L. Shang, W.Y. Wang, B.C. Zhou, Y. Wang, K.A. Darling, L.J. Kecskes, S.N. Mathaudhu, Z.K. Liu, Generalized stacking fault energy, ideal strength and twinnability of dilute Mg-based alloys: A first-principles study of shear deformation, Acta Mater. 67 (2014) 168–180.

[9] D. Zhang, H. Wen, M.A. Kumar, F. Chen, L. Zhang, I.J. Beyerlein, J.M. Schoenung, S. Mahajan, E.J. Lavernia, Yield symmetry and reduced strength differential in Mg-2.5Y alloy, Acta Mater. 120 (2016) 75–85.

[10] B. Yin, Z. Wu, W.A. Curtin, First-principles calculations of stacking fault energies in Mg-Y, Mg-Al and Mg-Zn alloys and implications for <c+a> activity, Acta Mater. 136 (2017) 249–261.

[11] T. Tsuru, D.C. Chrzan, Effect of solute atoms on dislocation motion in Mg: An electronic structure perspective, Sci. Rep. 5 (2015) 8793.

[12] K.-H. Kim, J.B. Jeon, N.J. Kim, B.-J. Lee, Role of yttrium in activation of <c+a> slip in magnesium: An atomistic approach, Scripta Mater. 108 (2015) 104–108.

[13] S.R. Agnew, M.H. Yoo, C.N. Tome, Application of texture simulation to understanding mechanical behavior of Mg and solid solution alloys containing Li or Y, Acta Mater. 49 (2001) 4277–4289.

[14] N. Stanford, R. Cottam, B. Davis, J. Robson, Evaluating the effect of yttrium as a solute strengthener in magnesium using in situ neutron diffraction, Acta Mater. 78 (2014) 1–13.

[15] E.M. Lauridsen, S. Schmidt, R.M. Suter, H.F. Poulsen, Tracking: a method for structural characterization of grains in powders or polycrystals, J. Appl. Crystallogr. 34 (2001) 744–750.

[16] H.F. Poulsen, S.F. Nielsen, E.M. Lauridsen, S. Schmidt, R.M. Suter, U. Lienert, L. Margulies, T. Lorentzen, D.J. Jensen, Three-dimensional maps of grain boundaries and the stress state of individual grains in polycrystals and powders, J. Appl. Crystallogr. 34 (2001) 751–756.

[17] H.F. Poulsen, Three-Dimensional X-ray Diffraction Microscopy. Berlin: Springer; 2004.

[18] H.F. Poulsen, An introduction to three-dimensional X-ray diffraction microscopy, J. Appl. Crystallogr. 45 (2012) 1084–1097.

[19] L. Margulies, T. Lorentzen, H. F. Poulsen, T. Leffers, Strain tensor development in a single grain in the bulk of a polycrystal under loading, Acta Mater. 50(2002) 1771–1779.

[20] R.V. Martins, L. Margulies, S. Schmidt, H.F. Poulsen, T. Leffers, Simultaneous measurement of the strain tensor of 10 individual grains embedded in an Al tensile sample, Mater. Sci. Eng. A 387 (2004) 84–88.

[21] J.V. Bernier, N.R. Barton, U. Lienert, M.P. Miller, Far-field high-energy diffraction microscopy: a tool for intergranular orientation and strain analysis, J. Strain Anal. Eng. Des. 46 (2011) 527–547.

[22] J. Oddershede, S. Schmidt, H.F. Poulsen, H.O. Sorensen, J. Wright, W. Reimers, Determining grain resolved stresses in polycrystalline materials using three-dimensional X-ray diffraction, J. Appl. Crystallogr. 43 (2010) 539–549.

[23] S. Schmidt, GrainSpotter: a fast and robust polycrystalline indexing algorithm, J. Appl. Crystallogr. 47 (2014) 276–284.

[24] J.C. Schuren, P.A. Shade, J.V. Bernier, S.F. Li, B. Blank, J. Lind, P. Kenesei, U. Lienert, R.M. Suter, T.J. Turner, D.M. Dimiduk, J. Almer, New opportunities for quantitative tracking of polycrystal responses in three dimensions, Curr. Opin. Solid State Mater. Sci. 19 (2015) 235–244.

[25] R. Pokharel, R.A. Lebensohn, Instantiation of crystal plasticity simulations for micromechanical modelling with direct input from microstructural data collected at light sources, Scripta Mater, 132 (2017) 73–77.

[26] T.J. Turner, P.A. Shade, J.V. Bernier, S.F. Li, J.C. Schuren, P. Kenesei, R.M. Suter, J. Almer, Crystal Plasticity Model Validation Using Combined High-Energy Diffraction Microscopy Data for a Ti-7Al Specimen, Metall. Mater. Trans. A 48 (2017) 627–647.

[27] W. Tang, K.L. Halm, D.R. Trinkle, M.K.A. Koker, U. Lienert, P. Kenesei, A.J. Beaudoin, A study of stress relaxation in AZ31 using high-energy X-ray diffraction, Acta Mater, 101 (2015) 71–79.

[28] C.C. Aydiner, J.V. Bernier, B. Clausen, U. Lienert, C.N. Tome, D.W. Brown, Evolution of stress in individual grains and twins in a magnesium alloy aggregate, Phys. Rev. B 80 (2009) 024113.

[29] T.R. Bieler, L.Y. Wang, A.J. Beaudoin, P. Kenesei, U. Lienert, In Situ Characterization of Twin Nucleation in Pure Ti Using 3D-XRD, Metall. Mater. Trans. A 45 (2014), 109–122.

[30] L. Wang, J. Lind, H. Phukan, P. Kenesei, J.-S. Park, R.M. Suter, A.J. Beaudoin, T.R. Bieler, Mechanical twinning and detwinning in pure Ti during loading and unloading - An in situ high-energy X-ray diffraction microscopy study, Scripta Mater. 92 (2014) 35–38.

[31] H. Abdolvand, M. Majkut, J. Oddershede, J.P. Wright, M.R. Daymond, Study of 3-D stress development in parent and twin pairs of a hexagonal close-packed polycrystal: Part I – in-situ three-dimensional synchrotron X-ray diffraction measurement, Acta Mater. 93 (2015) 246–255.

[32] T. Ungár, G. Ribárik, G. Zilahi, R. Mulay, U. Lienert, L. Balogh, S. Agnew, Slip systems and dislocation densities in individual grains of polycrystalline aggregates of plastically deformed CoTi and CoZr alloys, Acta Mater. 71 (2014) 264–282.

[33] J. Oddershede, J. P. Wright, A. Beaudoin, G. Winther, Deformation-induced orientation spread in individual bulk grains of an interstitial-free steel, Acta Mater. 85 (2015) 301–313.

[34] D.C. Pagan, P.A. Shade, N.R. Barton, J.-S. Park, P. Kenesei, D.B. Menasche, J.V. Bernier, Modeling slip system strength evolution in Ti-7Al informed by in-situ grain stress measurements, Acta Mater. 128 (2017) 406–417.

[35] L. Wang, Z. Zheng, H. Phukan, P. Kenesei, J.S. Park, J. Lind, R.M. Suter, T.R. Bieler, Direct measurement of critical resolved shear stress of prismatic and basal slip

in polycrystalline Ti using high energy X-ray diffraction microscopy, Acta Mater. 132 (2017) 598–610.

[36] Z. Huang, L. Wang, B. Zhou, T. Fischer, S. Yi, X. Zeng, Observation of non-basal slip in Mg-Y by in situ three-dimensional X-ray diffraction, Scripta Mater, 143 (2018) 44-48.

[37] U. Lienert, S. F. Li, C. M. Hefferan, J. Lind, R. M. Suter, J. V. Bernier, N. R. Barton, M. C. Brandes, M. J. Mills, M. P. Miller, B. Jakobsen, W. Pantleon, High-energy diffraction microscopy at the advanced photon source, JOM 63 (2011) 70–77.

[38] H. Sharma, R.M. Huizenga, S.E. Offerman, A fast methodology to determine the characteristics of thousands of grains using three-dimensional X-ray diffraction. I. Overlapping diffraction peaks and parameters of the experimental setup, J. Appl. Crystallogr. 45 (2012) 693–704.

[39] H. Sharma, R.M. Huizenga, S.E. Offerman, A fast methodology to determine the characteristics of thousands of grains using three-dimensional X-ray diffraction. II. Volume, centre-of-mass position, crystallographic orientation and strain state of grains, J. Appl. Crystallogr. 45 (2012) 705–718.

[40] https://www1.aps.anl.gov/Science/Scientific-Software/MIDAS

[41] G. Simmons, H. Wang, Single Crystal Elastic Constants and Calculated Aggregate Properties. A Handbook, second ed. Cambridge: The MIT Press; 1971.

[42] H. Wang, P.D. Wu, C.N. Tomé, Y. Huang, A finite strain elastic-viscoplastic self-consistent model for polycrystalline materials, J Mech Phys Solids 58 (2010) 594–612.

[43] R.A. Lebensohn, C.N. Tomé, A self-consistent anisotropic approach for the simulation of plastic deformation and texture development of polycrystals: Application to zirconium alloys, Acta Metall. Mater. 41 (1993) 2611–2624.

[44] H. Wang, P.D. Wu, C.N. Tomé, J. Wang, Study of lattice strains in magnesium alloy AZ31 based on a large strain elastic-viscoplastic self-consistent polycrystal model, Int. J. Solids and Struct. 49 (2012) 2155–2167.

[45] H. Wang, S.Y. Lee, M.A. Gharghouri, P.D. Wu, S.G. Yoon, Deformation behavior of Mg-8.5wt.%Al alloy under reverse loading investigated by in-situ neutron diffraction and elastic viscoplastic self-consistent modeling, Acta Mater 107 (2016) 404–414.

[46] H. Wang, B. Clausen, L. Capolungo, I.J. Beyerlein, J. Wang, C.N. Tomé, Stress and strain relaxation in magnesium AZ31 rolled plate: In-situ neutron measurement and elastic viscoplastic polycrystal modeling, Int J Plast. 79 (2016) 275–292.

[47] I.J. Beyerlein, C.N. Tomé, A dislocation-based constitutive law for pure Zr including temperature effects, Int J Plast. 24 (2008) 867–895.

[48] H. Wang, P.D. Wu, J. Wang, C.N. Tomé, A crystal plasticity model for hexagonal close packed (HCP) crystals including twinning and de-twinning mechanisms, Int J Plast. 49 (2013) 36–52.

[49] C.M. Cepeda-Jiménez, J.M. Molina-Aldareguia, M.T. Pérez-Prado, Effect of grain size on slip activity in pure magnesium polycrystals, Acta Mater. 84 (2015) 443–456.

[50] Kocks et al. Texture and Anisotropy. Cambridge: New York; 1998.

[51] B. Joni, T. Al-Samman, S.G. Chowdhury, G. Csiszar, T. Ungar, Dislocation densities and prevailing slip-system types determined by X-ray line profile analysis in a textured AZ31 magnesium alloy deformed at different temperatures, J. Appl. Crystallogr. 46 (2013) 55–62.

[52] C.J. Boehlert, Z. Chen, I. Gutiérrez-Urrutia, J. Llorca, M.T. Pérez-Prado, In situ analysis of the tensile and tensile-creep deformation mechanisms in rolled AZ31, Acta Mater. 60 (2012) 1889–1904.

[53] H. Wang, C.J. Boehlert, Q.D. Wang, D.D. Yin, W.J. Ding, In-situ analysis of the tensile deformation modes and anisotropy of extruded Mg-10Gd-3Y-0.5Zr (wt.%) at elevated temperatures, Int. J. Plast. 84 (2016) 255–276.

[54] J. Ye, R.K. Mishra, A.K. Sachdev, A.M. Minor, In situ TEM compression testing of Mg and Mge0.2 wt.% Ce single crystals, Scr. Mater. 64 (2011) 292–295.

[55] C.M. Byer, K. Ramesh, Effects of the initial dislocation density on size effects in single-crystal magnesium, Acta Mater. 61 (2013) 3808–3818.

[56] K.E. Prasad, K. Rajesh, U. Ramamurty, Micropillar and macropillar compression responses of magnesium single crystals oriented for single slip or extension twinning, Acta Mater. 65 (2014) 316–325.

[57] Y. Liu, N. Li, M. Arul Kumar, S. Pathak, J. Wang, R.J. McCabe, N.A. Mara, C.N. Tomé, Experimentally quantifying critical stresses associated with basal slip and twinning in magnesium using micropillars, Acta Mater. 135 (2017) 411–421.

[58] N. Stanford, M.R. Barnett, Solute strengthening of prismatic slip, basal slip and twinning in Mg and Mg–Zn binary alloys, Int. J. Plast. 47 (2013) 165–181.

[59] K. Chatterjee, A. Venkataraman, T. Garbaciak, J. Rotella, M.D. Sangid, A.J. Beaudoin, P. Kenesei, J.S. Park, A.L. Pilchak, Study of grain-level deformation and residual stresses in Ti-7Al under combined bending and tension using high energy diffraction microscopy (HEDM), Int. J. Solids and Struct. 94-95 (2016) 35–49.

[60] K. Chatterjee, J.Y.P. Ko, J.T. Weiss, H.T. Philipp, J. Becker, P. Purohit, S.M. Gruner, A.J. Beaudoin, Study of residual stresses in Ti-7Al using theory and experiments, J. Mech. Phys. Solids 109 (2017) 95–116.

[61] H. Abdolvand, J. Wright, A.J. Wilkinson, Strong grain neighbour effects in polycrystals, Nat. Commun. 9 (2018) 171.

[62] D. Naragani, M.D. Sangid, P.A. Shade, J.C. Schuren, H. Sharma, J.-S. Park, P. Kenesei, J.V. Bernier, T.J. Turner, I. Parr, Acta Mater, 137 (2017) 71–84.

Figures

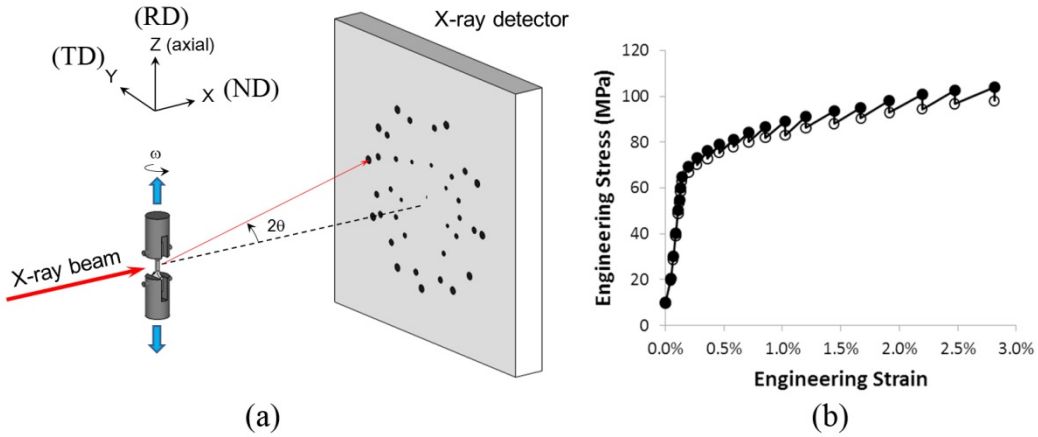

Fig. 1. (a) A schematic of the setup for in situ FF-HEDM experiment. The incoming X-ray (X direction) is parallel to the ND of the specimen; the tensile loading direction (Z) is parallel to the RD of the specimen. (b) Stress-strain curve from the in situ tensile test, in which the solid symbols represent the immediate flow stress in the specimen after each loading, and the open symbols represent the stress readout after the FF-HEDM measurement of each step.

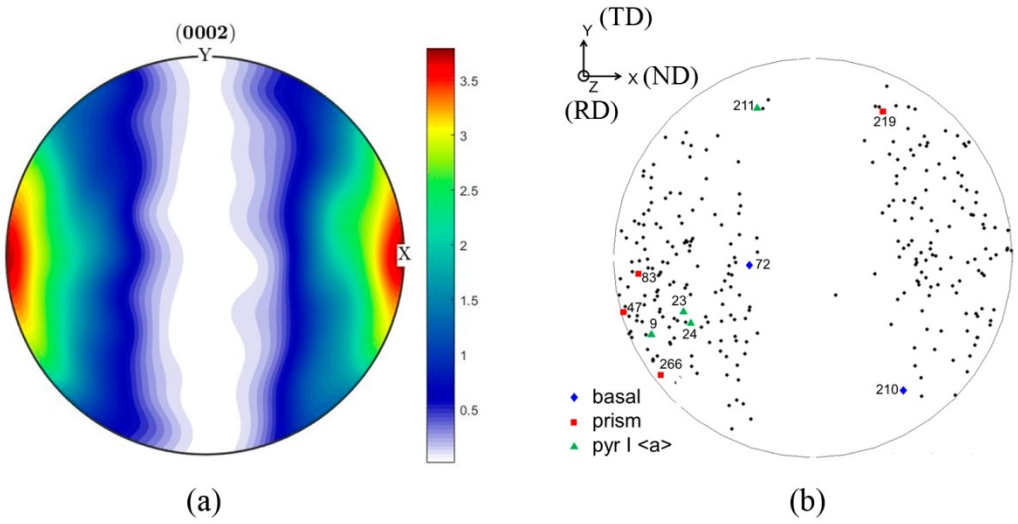

Fig. 2. (a) {0002} pole figure based on the 955 grain orientations from FF-HEDM indexation. (b) {0002} poles of the 286 grains that were tracked during deformation. Ten grains that show distinct evidence of basal slip, prismatic slip, or pyramidal I <a> slip are highlighted.

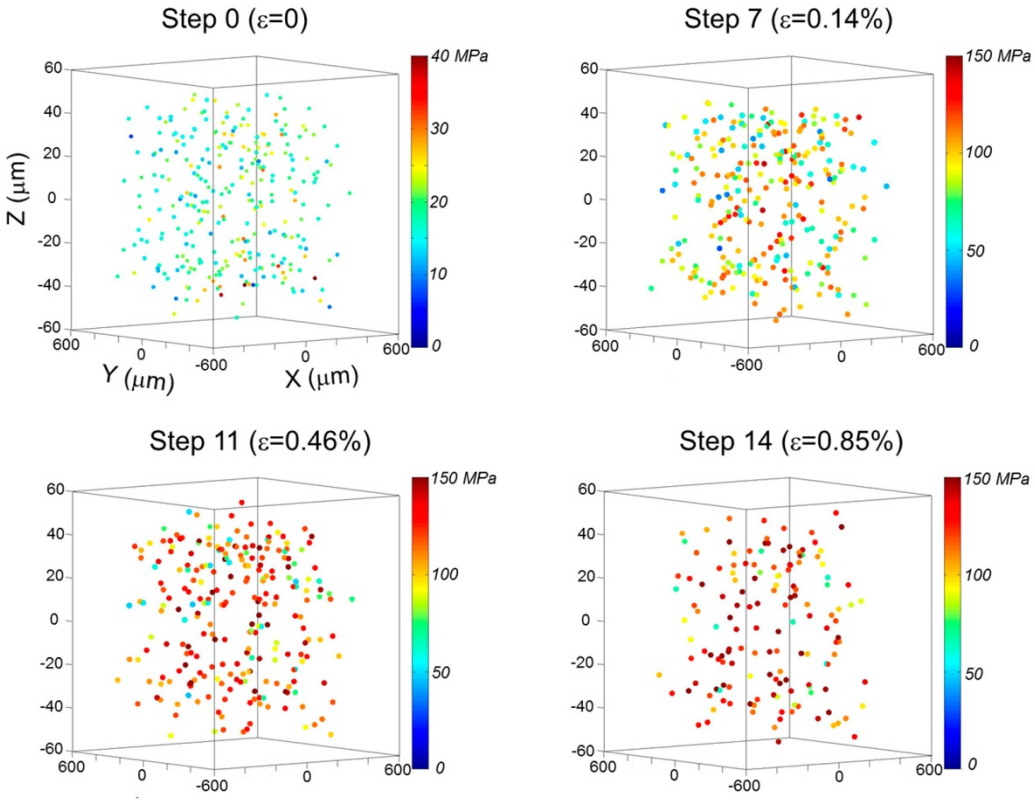

Fig. 3. COMs and evolution of the von Mises stress of the 286 grains. The COM of each grain is colored based on the instantaneous von Mises stress value.

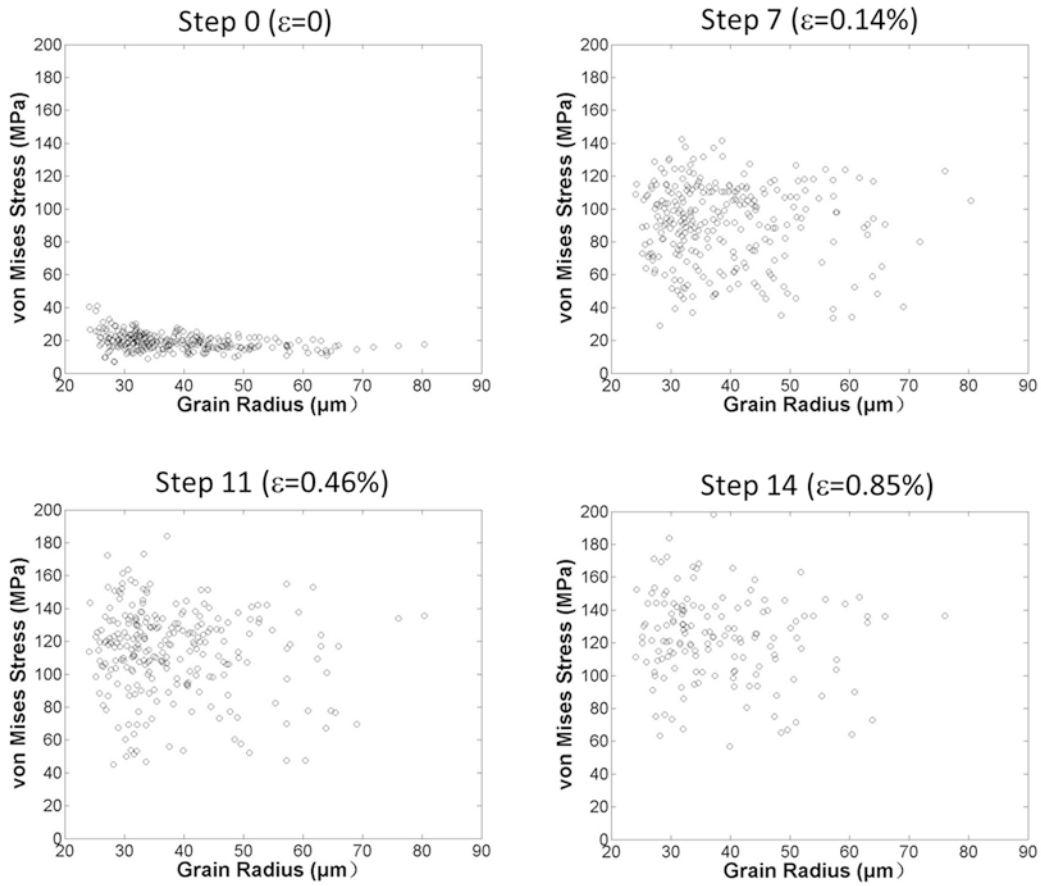

Fig. 4. Variation of σ_{VM} as a function of grain radius at different strains.

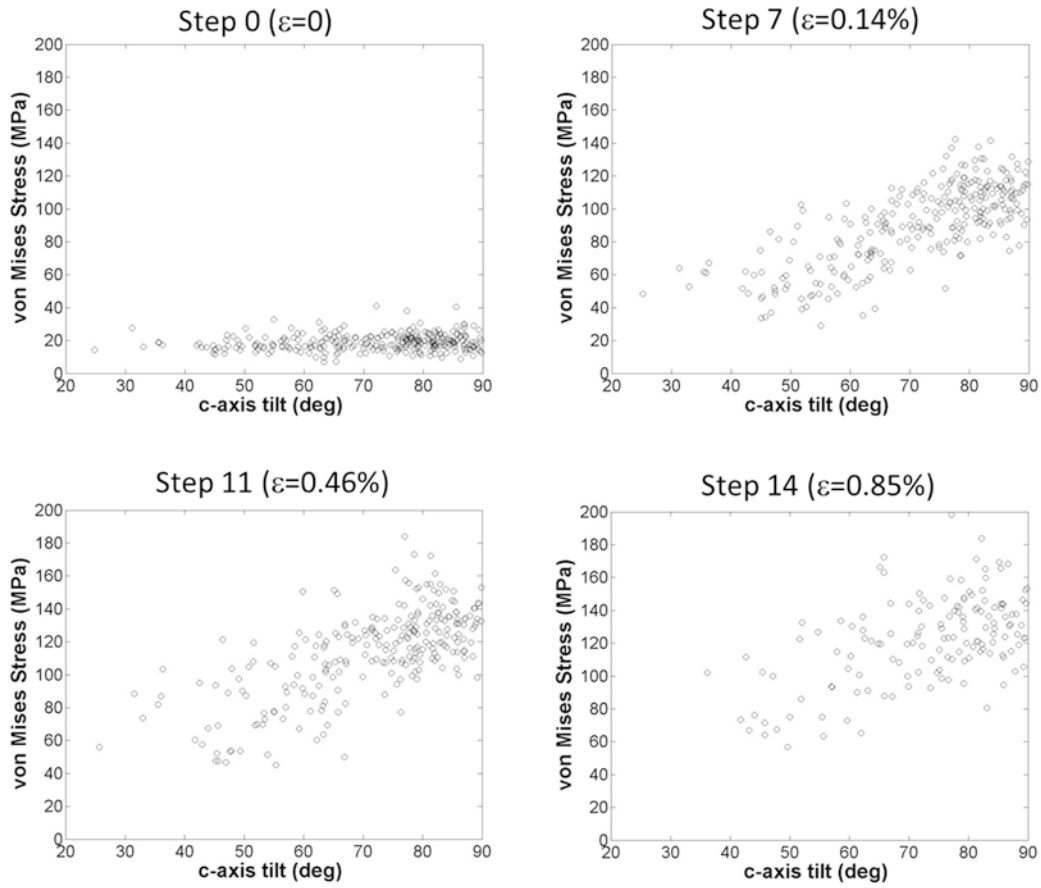

Fig. 5. Variation of σ_{VM} as a function of the angle between the c-axis of the grain and the loading direction Z (c-axis tilt) at different strains.

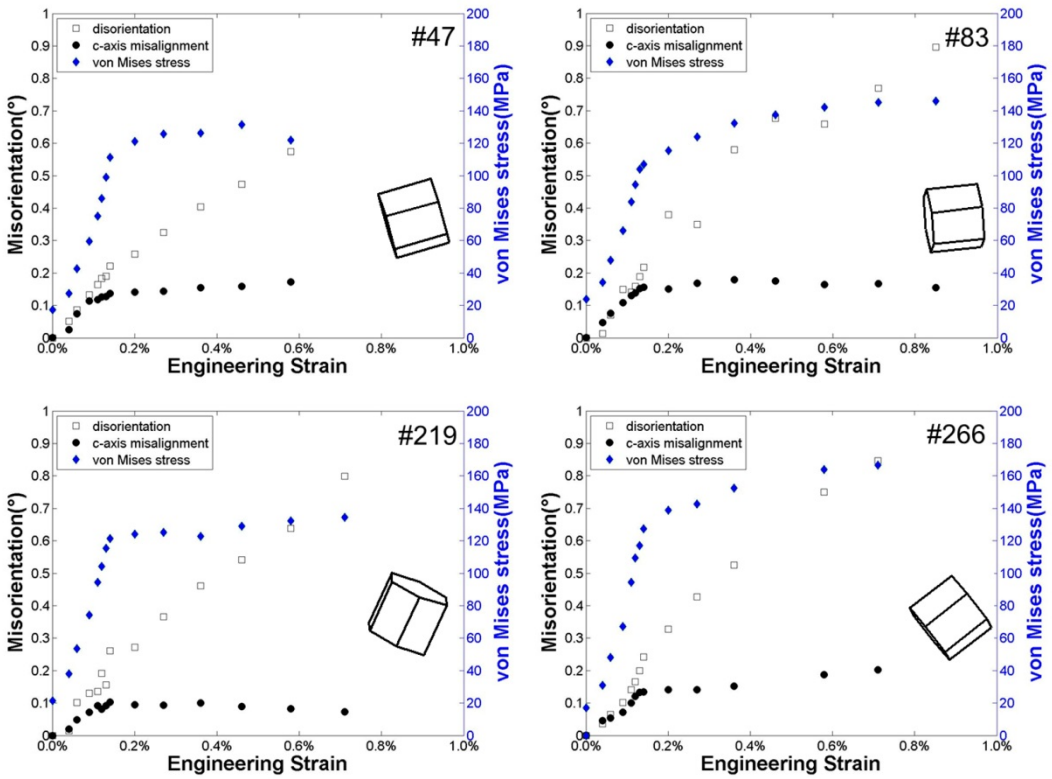

Fig. 6. Evolution of the disorientation, c-axis misalignment, and von Mises stress values in four grains that show prismatic slip activity. The initial orientation for each grain is represented by a hexagonal cell in the X-Y plane.

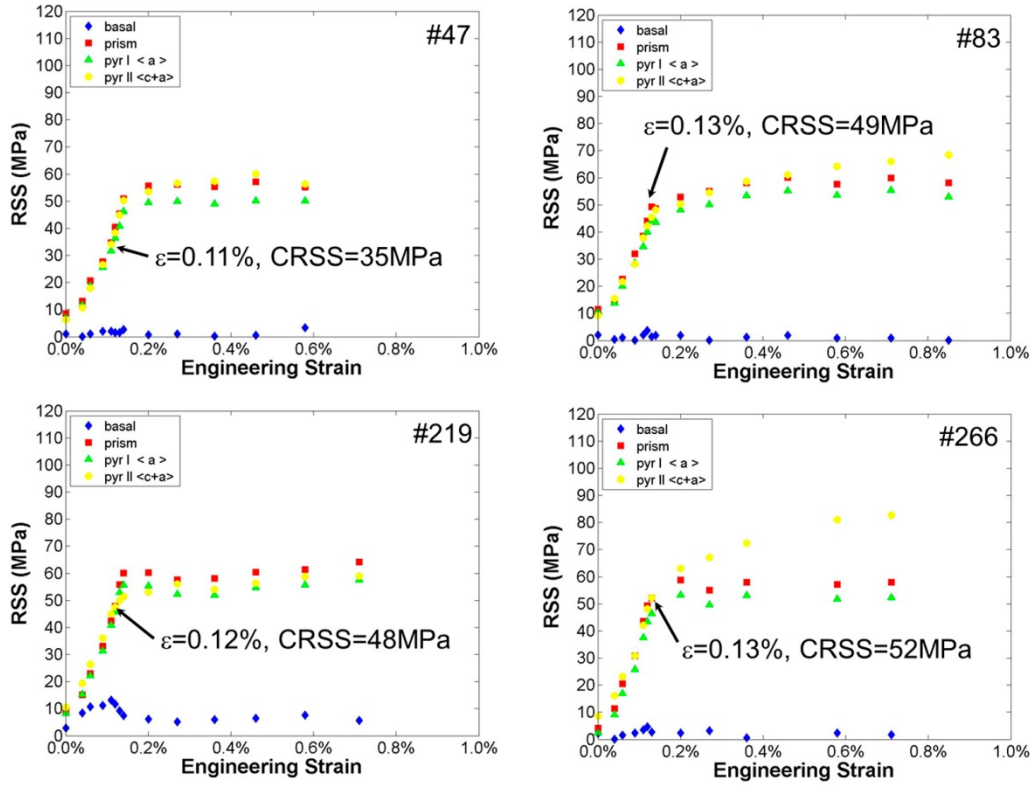

Fig. 7. Evolution of τ_{prism}, τ_{basal}, $\tau_{pyr\ I\ <a>}$, and $\tau_{pyr\ II\ <c+a>}$ in Grains 47, 83, 219, and 266 at different strains. The critical strain and CRSS for prismatic slip activation in each grain are shown.

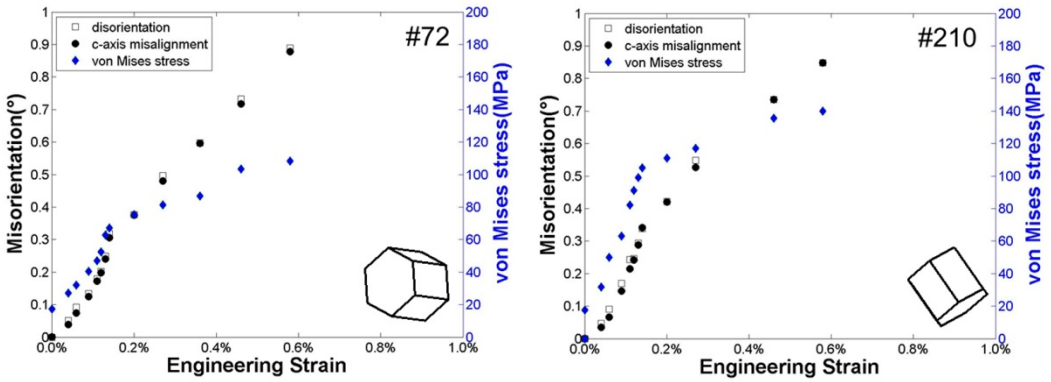

Fig. 8. Evolution of the disorientation, c-axis misalignment, and von Mises stress values in two grains that show basal slip activity. The initial orientation for each grain is represented by a hexagonal cell in the X-Y plane.

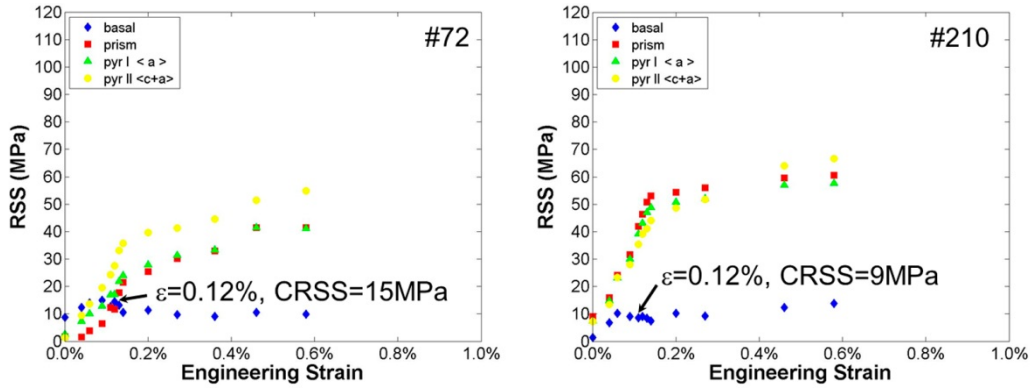

Fig. 9. Evolution of τ_{prism}, τ_{basal}, $\tau_{pyr\ I\ <a>}$, and $\tau_{pyr\ II\ <c+a>}$ in Grains 72 and 210 at different strains. The critical strain and CRSS for basal slip activation in each grain are shown.

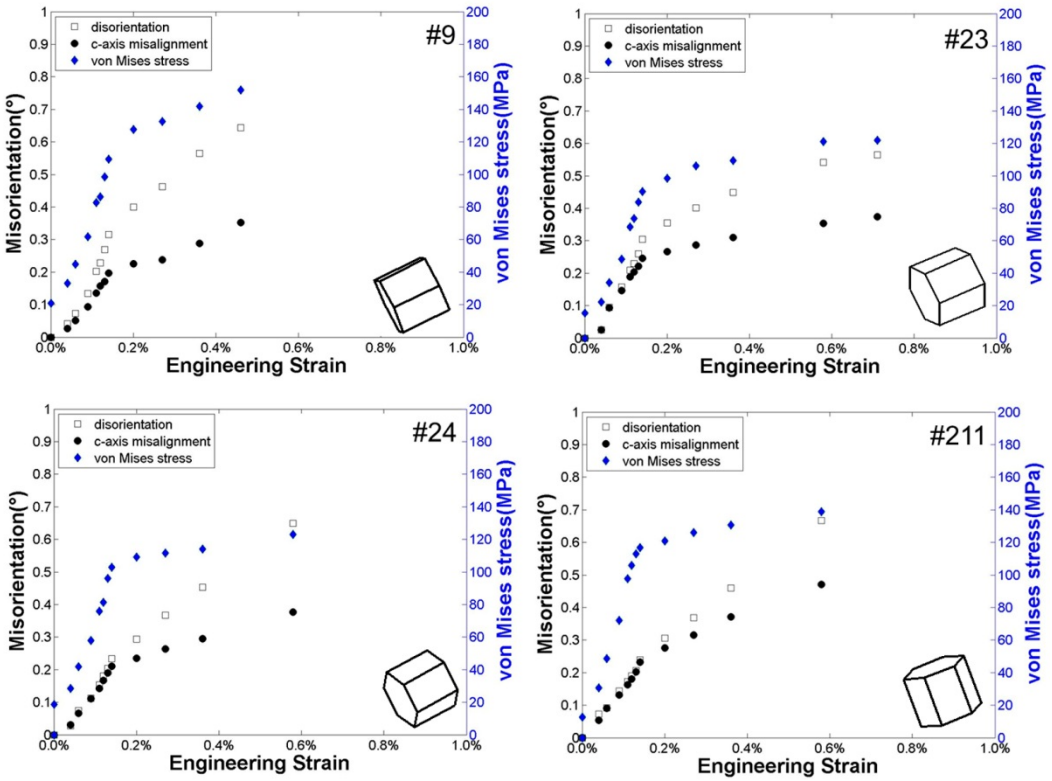

Fig. 10. Evolution of the disorientation, c-axis misalignment, and von Mises stress values in four grains that show pyramidal I <a> slip activity. The initial orientation for each grain is represented by a hexagonal cell in the X-Y plane.

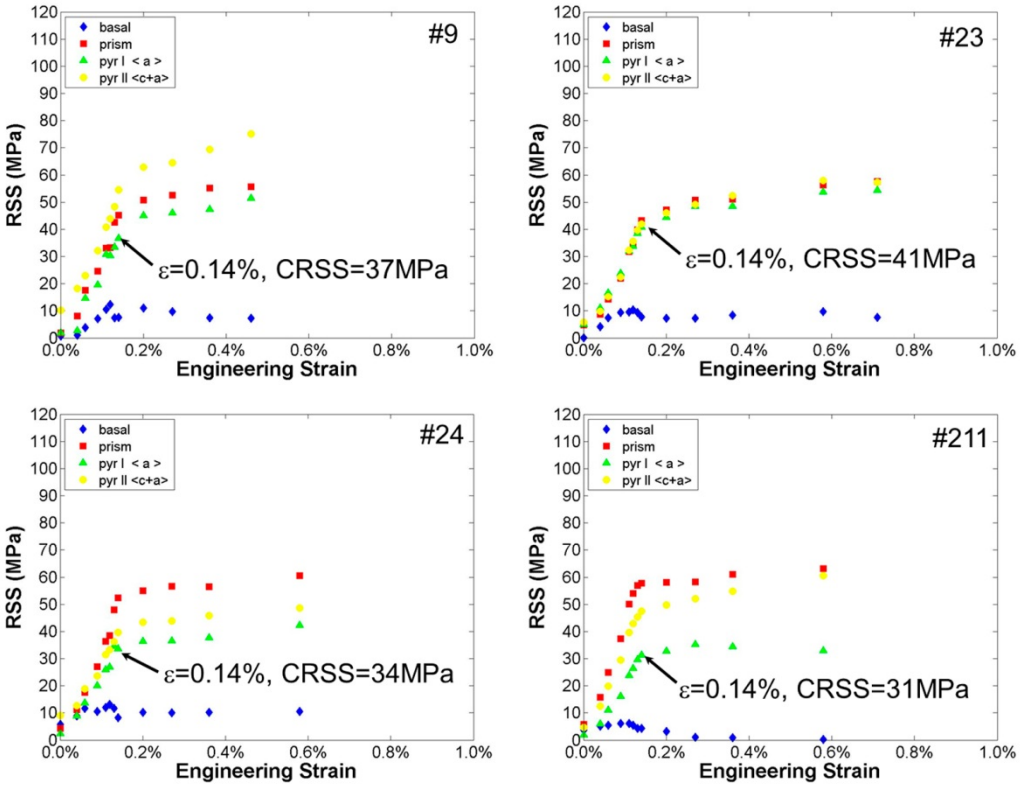

Fig. 11. Evolution of τ_{prism}, τ_{basal}, $\tau_{pyr\ I\ <a>}$, and $\tau_{pyr\ II\ <c+a>}$ in Grains 9, 23, 24, and 211 at different strains. The critical strain and CRSS for pyramidal I <a> slip activation in each grain are shown.

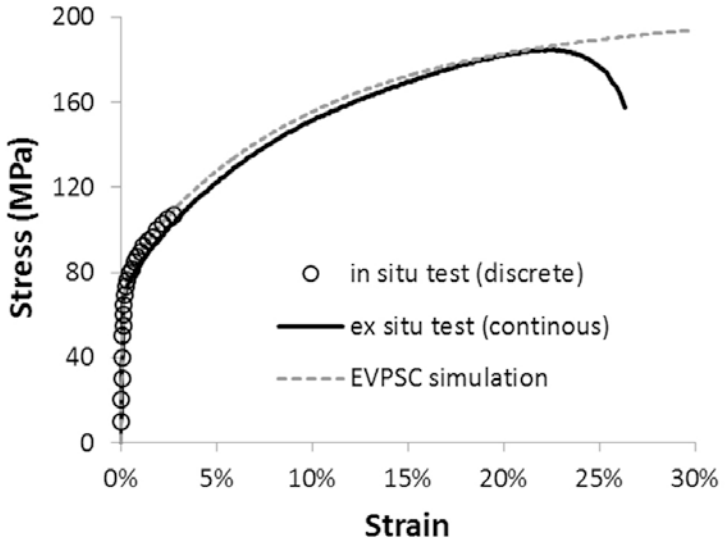

Fig. 12. Comparison of the simulated stress-strain curve by the EVPSC model with the stress-strain curves from the in situ test (discrete load steps) and the ex situ test (continuous loading).

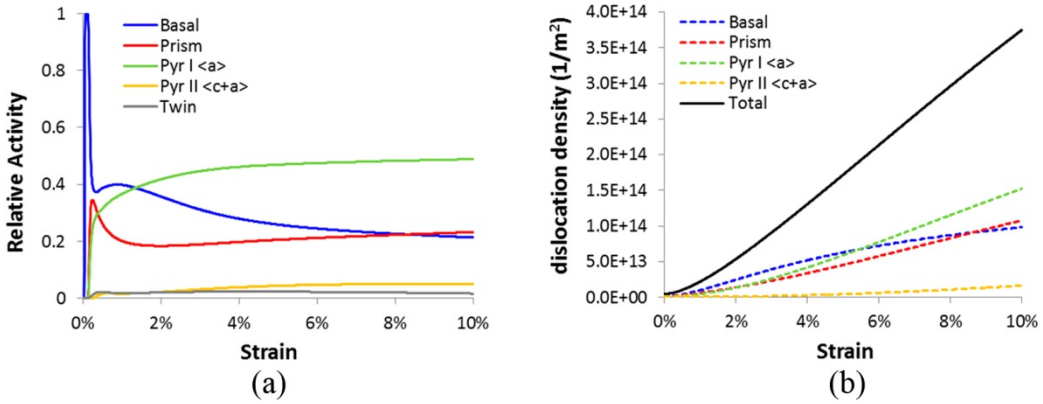

Fig. 13. (a) Relative activities of the five deformation modes as a function of the strain according to the EVPSC simulation. (b) The evolution of dislocation densities of the four slip modes as a function of the strain.

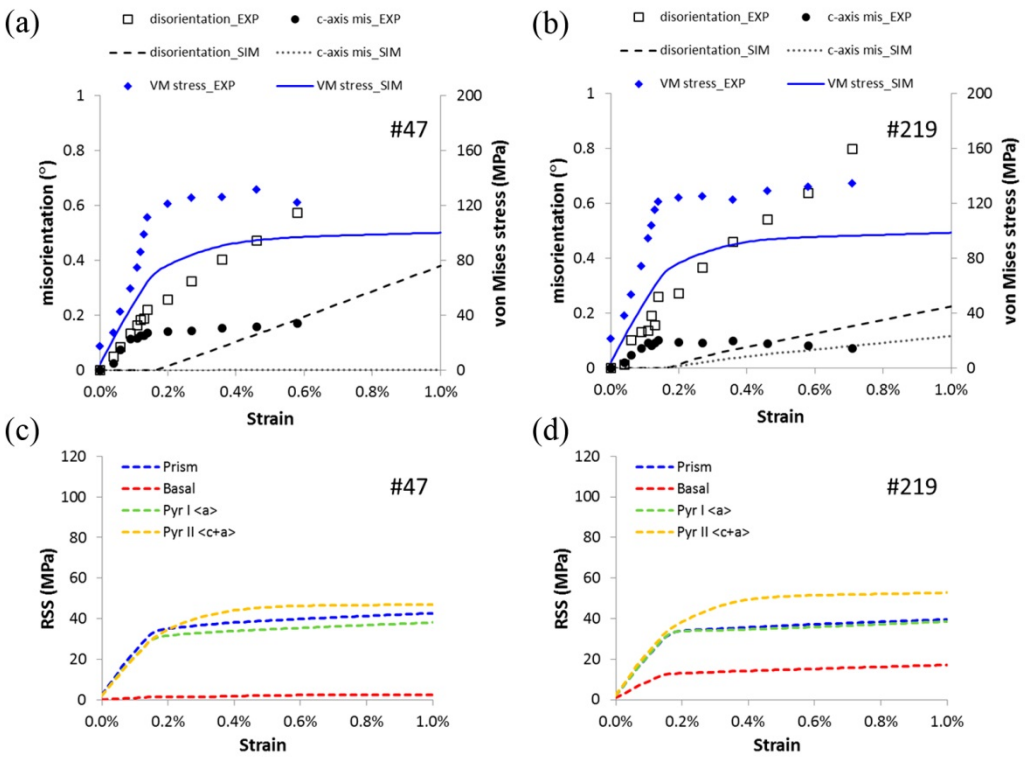

Fig. 14. (a, b) Simulated and measured evolution of the disorientation, c-axis misalignment, and von Mises stress values for Grain 47 and Grain 219. (c, d) Calculated evolution of τ_{basal}, τ_{prism}, $\tau_{pyr\ I\ <a>}$, and $\tau_{pyr\ II\ <c+a>}$ in Grain 47 and Grain 219.

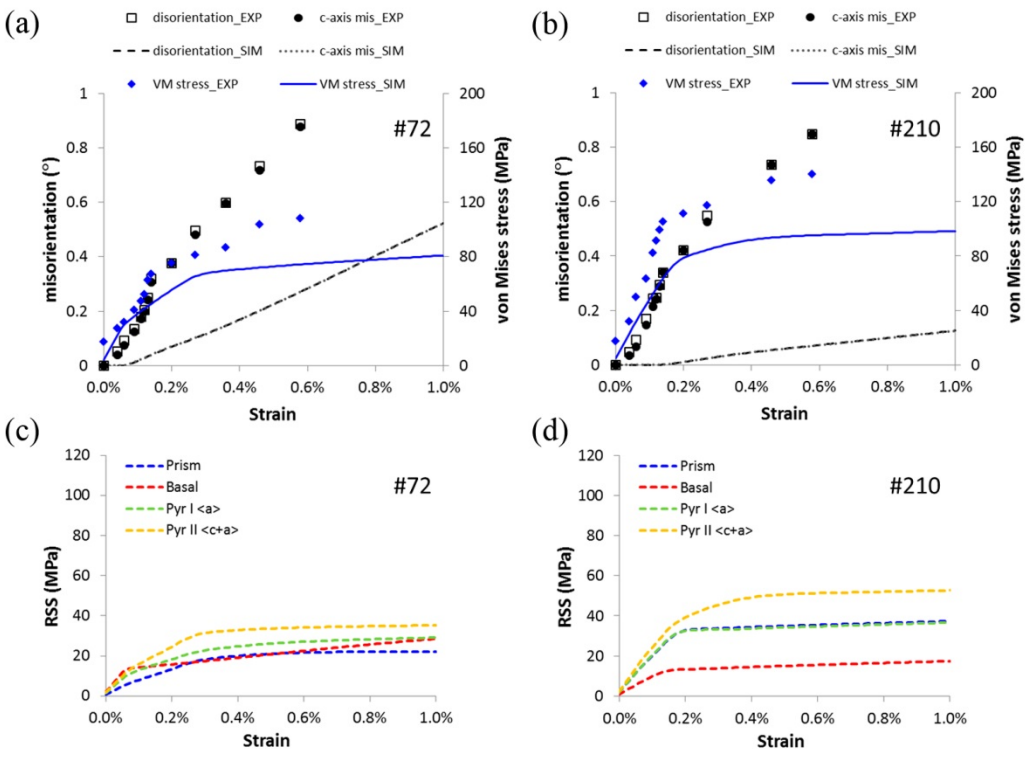

Fig. 15. (a, b) Simulated and measured evolution of the disorientation, c-axis misalignment, and von Mises stress values for Grain 72 and Grain 210. (c, d) Calculated evolution of τ_{basal}, τ_{prism}, $\tau_{pyr\ I\ <a>}$, and $\tau_{pyr\ II\ <c+a>}$ in Grain 72 and Grain 210.

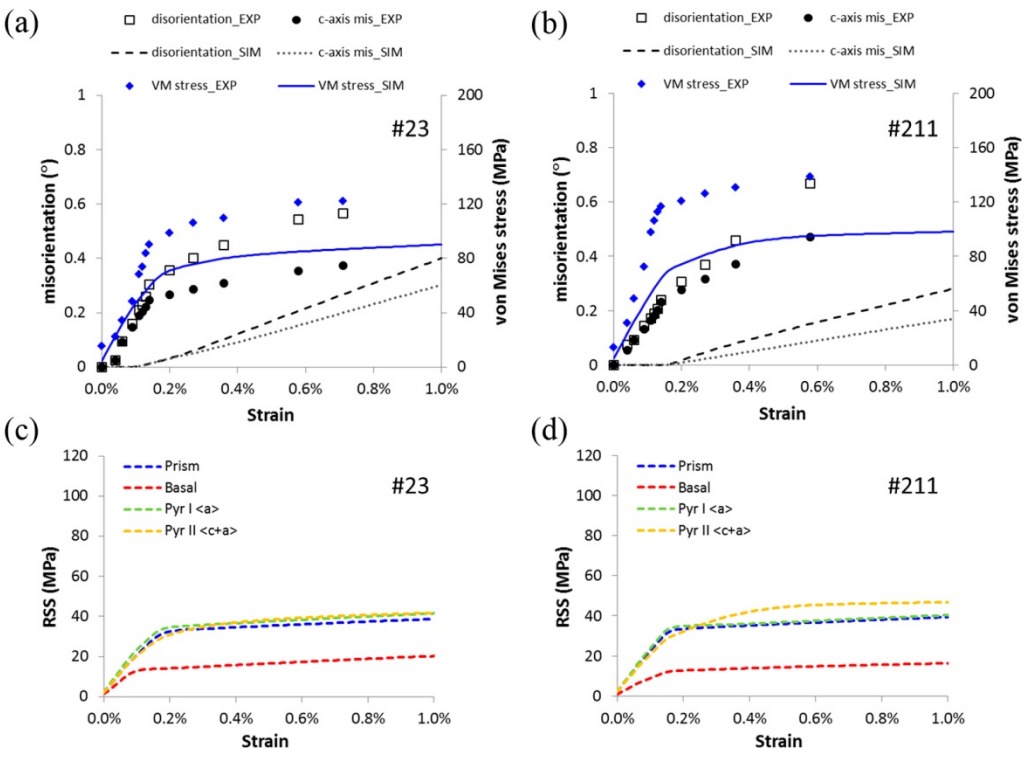

Fig. 16. (a, b) Simulated and measured evolution of the disorientation, c-axis misalignment, and von Mises stress values for Grain 23 and Grain 211. (c, d) Calculated evolution of τ_{basal}, τ_{prism}, $\tau_{pyr\ I\ <a>}$, and $\tau_{pyr\ II\ <c+a>}$ in Grain 23 and Grain 211.

Tables

Table 1. Parameters used in the dislocation-based EVPSC model.

	τ_0^α (MPa)	χ	b^α (Å)	ρ_0^α (m^{-2})	k_1^α (m^{-1})	g^α	D^α	n
Basal	12	0.9	3.21	4.3e11	6.6e8	0.6	20	20
Prismatic	38	0.9	3.21	4.3e11	8.0e8	0.6	20	20
Pyr I <a>	36	0.9	3.21	2.6e11	5.5e8	0.6	20	20
Pyr II <c+a>	60	0.9	6.12	1.7e11	8.7e8	0.8	20	20
Twinning	40	NA	NA	NA	NA	NA	NA	20